**RESEARCH ARTICLE**

Numerical Simulation of Ion Transport in a Nano-Electrospray Ion Source at Atmospheric Pressure

Wei Wang,[1,2] Steve Bajic,[2] Benzi John,[1] David R. Emerson[1]

[1]Scientific Computing Department, Science and Technology Facilities Council, Daresbury Laboratory, Sci-Tech Daresbury, Warrington, Cheshire WA4 4AD, UK
[2]Waters Corporation, Altrincham Rd, Wilmslow, Cheshire SK9 4AX, UK
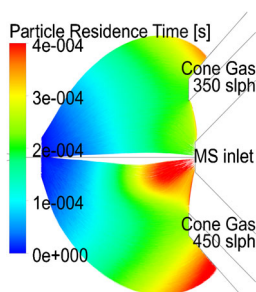
Abstract. Understanding ion transport properties from the ion source to the mass spectrometer (MS) is essential for optimizing device performance. Numerical simulation helps in understanding of ion transport properties and, furthermore, facilitates instrument design. In contrast to previously reported numerical studies, ion transport simulations in a continuous injection mode whilst considering realistic space-charge effects have been carried out. The flow field was solved using Reynolds-averaged Navier-Stokes (RANS) equations, and a particle-in-cell (PIC) method was applied to solve a time-dependent electric field with local charge density. A series of ion transport simulations were carried out at different cone gas flow rates, ion source currents, and capillary voltages. A force evaluation analysis reveals that the electric force, the drag force, and the Brownian force are the three dominant forces acting on the ions. Both the experimental and simulation results indicate that cone gas flow rates of ≤250 slph (standard liter per hour) are important for high ion transmission efficiency, as higher cone gas flow rates reduce the ion signal significantly. The simulation results also show that the ion transmission efficiency reduces exponentially with an increased ion source current. Additionally, the ion loss due to space-charge effects has been found to be predominant at a higher ion source current, a lower capillary voltage, and a stronger cone gas counterflow. The interaction of the ion driving force, ion opposing force, and ion dispersion is discussed to illustrate ion transport mechanism in the ion source at atmospheric pressure.

Keywords: Nano-ESI-MS, Ion transport, Space-charge effect, Numerical gas dynamic simulation

Introduction

Electrospray ionization mass spectrometry (ESI-MS) is a powerful analytical technique that provides both qualitative and quantitative information in chemical and biological applications [1–4]. MS with nano-electrospray ionization (nano-ESI) is an important branch of ESI sources [5–8]. A nano-ESI emitter has a micro-scale orifice that promotes low analyte consumption, which benefits the mass spectrometric analysis of analyte of limited availability. In a nano-ESI-MS, the analyte ionization is induced by applying a high DC voltage to the emitter at a variable distance from a counter electrode. After ionization, the charged droplets/ions are transported into the MS through the MS inlet. In addition to the electric driving force, drag force from the buffer gas at atmospheric pressure and the Coulombic repelling force lead to ion dispersion and

reduction of the ion transmission efficiency. These competing processes complicate the characteristics of the ion transmission. From an experimental perspective, it is difficult to measure the relative importance of the underlying mechanisms in ion transmission since the MS only records the "end product" of transmitted ions. Therefore, it is essential to implement numerical simulation tools in order to understand the transport properties of the ion source and, furthermore, to improve the efficiency of transfer of ions into the analyzer.

The detection limit of a mass spectrometer is highly dependent on the analyte ionization efficiency in the ion source and the ion transmission efficiency through the MS inlet. The analyte ionization efficiency is determined by several factors, including analyte type, analyte concentration, solvent composition, emitter design, etc. [9]. Owing to a number of unknowns in the ionization mechanism, it is difficult to quantify these influencing factors.

The ion transmission efficiency is the ratio of the ions that reach the MS detector to the total ions generated in the

Correspondence to: Wei Wang; *e-mail:* wei.wang@stfc.ac.uk

ionization process. The loss of ions during the ion transfer process to the MS detector can be large, and the majority are lost in the ion source [10], especially for atmospheric pressure ion sources. Factors influencing the ion transmission efficiency in the ion source include the applied voltage on the emitter, the source current, the gaseous flow field, the ESI-MS interface design, etc. This study will focus on the ion transport properties of the ion source at atmospheric pressure and will not consider the ion generation mechanism in the nano-ESI plume.

Studies of the ion transmission efficiency in ESI sources at atmospheric pressure have advanced in the past decade [11–13]. Experimental studies with different electrospray (ES) conditions have found that for low flow rate electrosprays, the decreased ES current reduces space-charge effects and increases the transmission efficiency [9, 14]. However, the generally divergent nature of the charged spray leads to a discrepancy between the plume size and the MS inlet size (limited by practical considerations), which ultimately limits the ion transmission efficiency. As the ion transmission efficiency in the ESI source is highly dependent on the geometric design of the ESI-MS interface, novel designs of the interface [15–17] were experimentally carried out to manipulate the flow field and to further increase the ion transmission. These experimental works reveal the dependence of the ion transmission efficiency on several factors, but details about characteristics of ion transport from an atmospheric pressure ion source still need further study.

In addition to experimentation, numerical simulation is an alternative and potentially powerful tool due to its relatively low cost, short turnaround time, flexibility to change geometric and operating conditions, and reliable results. Numerical simulation of ion trajectories overcomes limited measurements in experiments to provide a full picture of ion transport properties and, furthermore, facilitates instrument design. However, numerical simulation is still challenging owing to the contradictory relationship between accuracy and computational cost in solving the full governing equations of particle motion under combined gas dynamics and electric forces. Transport of ions in a combined electric field and buffer gas field can be described by treating the ions as either a continuum (e.g., a scalar field of the ion concentration) or discrete particles. From a macroscopic perspective, an electro-kinetic transport equation, the Poisson-Nernst-Planck (PNP) equation, is applied to describe dynamics of the ion flux in a buffer gas and a weak electric field [18, 19]. From a microscopic perspective, motions of ions can be tracked individually in a discrete model, which is the particle tracking method. Based on different particle representations and treatments of buffer gas field, particle tracking methods can be combined with a continuous buffer flow field in the Euler-Lagrange approach. If both the tracking particles and the buffer gas molecules are treated as individual particles, the direct simulation Monte-Carlo (DSMC) method can be adopted to simulate the ion-gas collisions directly [20–22]. As the PNP equation for a continuous ion concentration field is not as stable and numerically reliable as particle tracking methods [19, 23], it is rarely applied to the field of mass spectrometry. The DSMC method suffers from prohibitively expensive computational cost at an elevated pressure of the buffer gas. When it is used in an ESI-MS system, it is usually combined with a computational fluid dynamics (CFD) method for the ion source at atmospheric pressure [24]. For the Euler-Lagrange approach with discrete particles and a continuous buffer gas field, the interaction between the ion and the buffer gas can also be calculated by several different methods. One is to use the viscous damping method (the Stokes' drag law) to describe the net effect of buffer gas on the particles [25], for example, the discrete phase model (DPM) [26] in ANSYS Fluent. The Stokes' drag law, however, does not accurately represent the forces on particles of submicron-scale at high particle Knudsen numbers. A corrected drag law has been considered in this work and will be discussed in detail in the following section on methods. In order to consider the diffusional effects for ion transport, a statistical diffusion simulation (SDS) was introduced [27, 28] to account for both the ion mobility-based drift and random diffusion. The SDS method employs user-defined ion mobility or a predetermined field-dependent ion mobility function to achieve an average drift motion of ion and uses collision statistics to simulate hard-sphere collision-based diffusion of ions. With this method, the combined effect of mobility and diffusion on ion trajectories at a wide pressure range can be predicted with affordable computational resources. It has some applications in the MS system [17, 29]. Another method in the Euler-Lagrange frame is a hard-sphere collision-based Monte Carlo approach [30] to simulate ion-gas collision in a continuous buffer gas field, which is different from the DSMC method with collisions between discrete ion particles and buffer gas molecules. This Monte-Carlo method is widely used in ESI-MS systems [31, 32]. However, under atmospheric pressure conditions, the Monte-Carlo method is computationally prohibitive for a continuous injection of ions due to the extremely high ion-gas collision frequency at elevated pressures.

There are several commercial software packages for ion tracking in an MS system. The ion optics simulation software, SIMION [33–35], is a common tool used in the MS industry to solve gas-phase ion transport. Nevertheless, SIMION cannot solve the gaseous flow field but relies on the flow variables to be imported from an external CFD solver. COMSOL Multiphysics is another simulation tool commonly used in MS [24, 32, 36, 37]. It is based on a finite element method, which has limited numerical techniques to accurately solve very complex flows. For an ion source at atmospheric pressure involving complex flow and electric fields, both impacting the motions of ions, CFD solvers such as ANSYS Fluent with customized functionality is an excellent choice for ion transport simulations. ANSYS Fluent simulations of MS at atmospheric pressure have been reported previously [31, 38]. A major advantage of these approaches is that it is capable of computing ion trajectories within any arbitrary 2D or 3D geometry under the combined influence of complex gaseous flow and electric field using a single software package.

In order to take account of the space-charge effects, SIMION introduces a charge repulsion method based on

empirical estimations for an ion beam or ion cloud. This method is also adopted by Jurcicek et al. [31] in their ANSYS Fluent simulation. Another method is to apply an analytical expression for the Coulomb force for a simple geometry [39], which cannot, however, be extended for arbitrary geometries as in the case of an ion source chamber. Therefore, most of the previously published numerical works simulated a fixed initial ion number and distribution (single pulsed injection), where only the ion transport is captured and the real space-charge effects are most likely to be inaccurate due to the lack of a realistic ion distribution that would result from a continuous injection of ions. In this numerical study, ANSYS Fluent was customized to simulate ion trajectories, taking account of realistic space-charge effects in a continuous injection mode of nano-ESI in a cone-gas influenced ion source flow field. Using the developed methods, electric field distortion by space-charge effects and the ion transmission efficiency at different cone gas flow rates, capillary voltages, and the source currents were areas of focus for the study. Experiments were also carried out to complement and validate the simulations, wherever possible.

Methods

The Governing Equations

ANSYS Fluent is a commercial CFD software package based on the finite volume method to discretize partial differential equations for complex arbitrary geometries. It allows users to customize functionalities to enhance its capabilities with the aid of user-defined functions (UDF), user-defined material properties, user-defined particle injection files, etc. The governing equations for the flow field are the conservation equations of mass, momentum, and energy [26]. In the current study, a compressible turbulent flow is modeled using a Reynolds-Averaged Navier-Stokes (RANS) method. The density-based solver is chosen because of a rapid change of pressure and temperature that occurs near to the MS inlet and the k-ε turbulence model with an enhanced wall treatment is applied to capture turbulence statistics. The second order upwind scheme is used to discretize the convection terms in the governing equations. The library "Metis" [40] is applied for partitioning the computational domain for parallel computation.

The electric field is solved using the Poisson equation and the divergence relationship between the electric potential ϕ and electric field $\overrightarrow{E}$ (a three-dimensional vector), such that:

$$\nabla^2 \phi = -\frac{\rho_e}{\varepsilon_0};$$
$$\overrightarrow{E} = -\nabla \phi \tag{1}$$

where 'ρ_e' is the charge density, which is dependent on the real-time ion distribution, and 'ε_0' is the permittivity of free space. The Poisson equation is solved as a scalar transport equation using a user-defined scalar in ANSYS Fluent. The charge density in Equation 1 is calculated by the implementation of the

particle-in-cell (PIC) method [41] using a UDF. For the MS source study, the self-induced magnetic field is negligible; thus, it is assumed that the charged particles are not subjected to the self-induced magnetic field so that the Lorentz force is ignored and the binary interaction between charged particles is the Coulomb force. The PIC method is a technique to calculate both the static electric force and space-charge effects on charged particles in continuous phase space, which is a speed-up of the calculation directly by Coulomb's law. In the PIC method, the continuous electric potential field distorted by space-charge effects is directly calculated with a source of charge density. The charge density in the first-order discretization is a simple average of the charge carried by all particles located in a control element with the control volume. A higher-order discretization can be achieved by distributing the charge to computational nodes of the control element via a higher-order scatter operation. Herein, the first-order calculation is used for charge density with a mesh-independent study, which is recommended to reduce numerical errors for electric fields with a low charge density.

The motion of ions in a mass spectrometer ion source at atmospheric pressure is governed mainly by forces from the gas flow field, the electric field, and the space-charge effects. The forces on ions from the gas flow field can be modeled either using gas-ion collision models or suitable drag force models. The kinetic hard-sphere collision models typically used for computing ion-molecule collisions are suited to only low pressure (vacuum) conditions. At atmospheric pressure, the collision frequency is extremely high and the time step involved is extremely small, so that the associated computational cost for ion transport modeling in realistic geometries is prohibitively high, even using the fastest computers. In this study, focusing on the ion source chamber at atmospheric pressure, the drag forces and other forces from the gas flow field are calculated explicitly. The Lagrangian discrete phase model in ANSYS Fluent is applied to model ion transport in continuous injection mode under an unsteady electric field and a steady flow field.

The Lagrangian governing equation of a particle is:

$$\frac{d\overrightarrow{u}_p(\overrightarrow{x},t)}{dt} = -\frac{\overrightarrow{u}_p(\overrightarrow{x},t) - \overrightarrow{u}_g(\overrightarrow{x})}{\tau_p} + \frac{\overrightarrow{E}(\overrightarrow{x},t)q_p}{m_p} + \overrightarrow{f}_o \tag{2}$$

where the subscript 'p' stands for a particle, and 'g' for the buffer gas. The first term on the right-hand side (RHS) is the drag force from the particle's surrounding fluid, whereas the variable 'τ_p' is the particle relaxation time, and 'u' is the velocity vector. The second term on the RHS is the electric force on charged ions, whereas 'E' is the electric field vector, and 'q' is the charge carried by a particle. The last term 'f_o' represents the sum of all other forces acting on the particles, mainly including the Brownian force, the Saffman lift force, thermophoretic force, and turbulence dispersions.

A schematic of the entire simulation procedure is shown in Figure 1. First, the gaseous flow field of the ion source domain is solved using a RANS model. The static electric field is solved using the Laplace equation. Next, with the computed charge
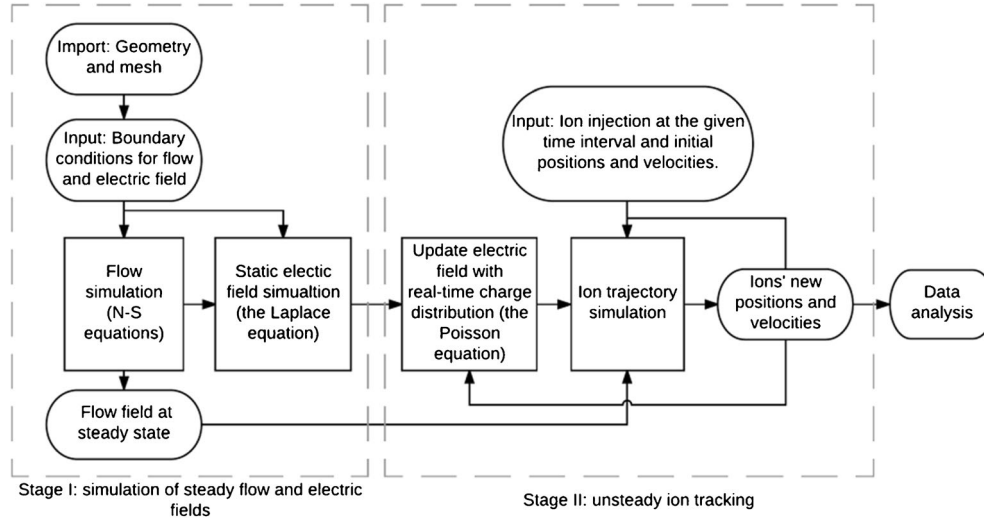
Figure 1. Schematic of the ion transport simulation procedure

density distribution from the last iteration, the Poisson equation is solved to obtain a space-charge distorted electric field. Subsequently, a Lagrangian particle tracking method is applied to calculate and update ion velocities and positions under a frozen flow field and the updated (time-dependent) electric field.

Validation of the Corrected Drag Model for Gas--Phase Ions

Although there are a few applications of drag force models with slip correction factors for nano/submicron particles [42, 43], their use in MS source modeling is still very rare compared with the Monte-Carlo method with a hard-sphere collision model [30]. In order to overcome the limitation of the stick boundary conditions in Stokes' drag model and to make it applicable to submicron particles of a higher Knudsen number, the Cunningham slip correction factor [44] is introduced as:

$$C = 1 + \text{Kn}\left[A + Be^{-E/\text{Kn}}\right] \tag{3}$$

where the Knudsen number Kn is the ratio of the mean free path λ and the particle diameter d_p. The parameters A, B, and E can be found in Li and Wang [45]. The particle drag in the corrected Stokes' drag model related to Reynolds number, Re, follows the suggestions in Clift et al. [46], in which the particle relaxation time with a local Reynolds number is expressed as:

$$\begin{cases} \tau_p = C \cdot \dfrac{d_p^2 \rho_p}{\mu_g} \cdot \dfrac{1}{18}, & if \ \text{Re} < 0.01 \\[2mm] \tau_p = C \cdot \dfrac{d_p^2 \rho_p}{\mu_g} \cdot \dfrac{1}{18 + 2.367 \text{Re}^{0.82 - 0.05\log_{10}\text{Re}}}, & if \ 0.01 < \text{Re} < 20.0 \\[2mm] \tau_p = C \cdot \dfrac{d_p^2 \rho_p}{\mu_g} \cdot \dfrac{1}{18 + 3.383 \text{Re}^{0.6305}}, & if \ 20.0 < \text{Re} < 260.0 \end{cases} \tag{4}$$

The drag model up to a Reynolds number of 10^6 can be found in Table 5.2 of Clift et al. [46].

In order to assess the feasibility of the drag model on nano-particles in the MS source, the ion mobility in a drift tube by both the corrected drag model and the Monte-Carlo model with hard-sphere collisions were studied. Two test cases have been considered for this validation study. The first case is to inject 20 ions of mass 70 Da into the buffer gas of nitrogen (N_2) at 273 K and 0.1 atm, which is the same as in [30] with a known collisional cross-section of 103.5 Å^2. The second case is to inject verapamil of a singly charged $(M+H)^+$ ion mass 455.6 Da into nitrogen at 293 K and 1 atm and the experimentally determined collisional cross-section of verapamil and nitrogen is 210.0 Å^2 [47]. Based on this collisional cross-section, an estimation of the ion mobility in the first Chapman-Enskog approximation under the assumption of the hard-sphere collision and a low electric field, the so-called Mason-Schamp equation [48, 49], is provided as a reference. (The contribution of the second-order approximation to the first order is about 2% [50].) The ion mobility predicted by the Mason-Schamp equation is:

$$K = \frac{(18\pi)^{\frac{1}{2}}}{16} \frac{ze}{(\kappa_b T)^{\frac{1}{2}}} \left(\frac{1}{m_i} + \frac{1}{m_g}\right)^{\frac{1}{2}} \frac{1}{N} \frac{1 + \alpha}{\Omega} \tag{5}$$

and the reduced ion mobility is defined as:

$$K_0 = K \frac{P}{P_0} \frac{T_0}{T} \tag{6}$$

where 'P_0' and 'T_0' are the standard temperature and pressure (STP); 'ze' is the ion charge; 'κ_b' is the Boltzmann constant; 'T' is the buffer gas temperature; 'm_g' is the molecular mass of the buffer gas; 'm_i' is the molecular mass of the ion; 'Ω' is the collisional cross section; 'N' is the number density of the buffer gas; 'α' is a correction factor, $\alpha < 0.02$ when $m_i > m_g$. It is to be noted here that Mason-Schamp equation has limitations due to the absence of elastic scattering attributable to long-range inter-molecular forces (e.g., the van der Waals interaction) and the ion-induced dipole interactions.

The reduced ion mobility is summarized in Table 1. Simulation results show that both methods in both cases display a reduced ion mobility that is independent of the electric field for fields lower than 500 V/cm. Both the collision model and the drag model predicted slightly greater ion mobility than the Mason-Schamp equation. The discrepancy by the drag model (<9%) is higher than that by the collision model (<6%) in both m/z 70 and m/z 455 cases. A possible reason for higher ion mobility by simulations is the underprediction of ion diffusion with only a few ions injected and correspondingly a higher drift velocity. Another reason for the discrepancy is the numerical errors with a second-order time discretization. The drag model predicted only a slightly greater discrepancy than the collision model (~3%), which is acceptable and preferable due to its high cost-performance. This validation study shows that the drag model with the Cunningham slip correction can predict relatively accurate ion transport properties in a MS source chamber at atmospheric pressure.

Results and Discussion

Computational Model and Configuration

A 2D axisymmetric simulation is carried out for the nano-ESI-MS source. A schematic of the nanospray source chamber considered is shown in Figure 2. The computational domain has a cone gas inlet with a specified mass flow rate, a pressure outlet of 1 atm at the far field, and a pressure outlet of 0.4 atm at the MS inlet. It should be noted that it is conventional to switch off the cone gas flow in standard nano-ESI-MS operation. However, the cone gas flow is included in this study since it provides a means of validating the model and expands our understanding of gas flows in relation to ion transport. In this study, the cone gas flow rate ranges from 0 to 450 slph. All other boundaries are no-slip walls. The MS inlet has a diameter of 0.8 mm and is offset by 0.2 mm from the cone gas orifice with a diameter of 3 mm. The nano-ESI capillary has a length of 25 mm and a tip orifice diameter of 2 μm. The distance between the capillary tip and the MS inlet is 5.2 mm. A high voltage is applied to the capillary, and all other solid walls are grounded. A very fine structured mesh of around 1 million cells is generated to capture the emitter tip geometry, which has been found to provide mesh-independent accuracy for the charge density calculation in the PIC method.

Because of a faster desolvation rate in nano-ESI compared with conventional ESI, this study makes an initial assumption as in previous studies [3] that fully desolvated gas-phase ions are instantaneously produced at the emitter tip. The gas-phase ion injection frequency is 10 MHz for a continuous injection mode. This injection interval is about one-thousandth of a typical transmission time for ions in a nano-ESI. After a study of different injection time intervals, the current one is validated to generate an effectively continuous injection. Based on the shape of a nano-ESI spray plume observed in experiments [51], the injected verapamil ions ($m/z = 455.6$, charge state = +1) were initially randomly seeded in a circular plane with a radius of 0.5 mm and located 0.5 mm in front of the emitter tip. The velocity of particles is initialized to follow the Maxwell-Boltzmann particle velocity distribution.

All simulations in this work were performed in parallel mode using Open MPI [52] on an IBM iDataPlex system called the *Blue Wonder*. *Blue Wonder* is located at the Hartree Center in the UK, and each node in this system consists of 2×12 core Intel Xeon processors (Ivy Bridge E5-2697v2 2.7GHz) and 64GB RAM. Each parallel simulation case in this study used 32 cores. The computational time mostly depends on the number of tracking ions existing in the source chamber. For example, for the case with an ion source current of 30 nA, a cone gas flow rate of 50 slph, and a capillary voltage of 2 kV, the transient physical time to reach the equilibrium state is about 0.2 ms and the equilibrium tracking particle number is about 10,000. For this case, it took around 6.5 h of wall-clock time with 32 cores to reach the equilibrium state. Upon reaching equilibrium, it took about 0.5 h of wall-clock time to advance 0.01 ms of physical time in the unsteady particle tracking.

Flow Field

The flow field is determined by a combination of the low pressure at the MS inlet and the counter-current flow of the cone gas. The exact pressure at the MS inlet is unknown beforehand, as it is related to the pressure in the first vacuum region of the MS. MS inlet pressures from 0.1 to 1 atm have been studied, and show that if the pressure is lower than approximately 0.45 atm in the current configuration, the velocity profiles in the dominant region of the source chamber show no discernible differences due to choked flow at the MS inlet. A gas flow study of a different type of nanospray ESI source (a heated capillary connecting the atmosphere and a fore-vacuum volume) [53] found that MS inlet pressures lower than around 0.4 atm had little influence on the mass flow rate into the MS. In order to rule out the influences of the MS inlet pressure on flow field and to focus on the flow field in the source chamber only, a pressure of 0.4 atm at the MS inlet in this study was chosen.

When the pressure at the MS inlet is fixed at 0.4 atm, the computed axial velocity profiles at different cone gas flow rates are shown in Figure 3. It is observed that the flow velocity rapidly increases up to 280 m/s near the MS inlet (i.e., x = −0.002 m, not shown) at all studied cone gas flow rates. The

Table 1. Reduced Ion Mobility of Ions in a Drift Tube. The Simulation Data has been Computed Using Electric Fields of 100, 200, 300, 400, and 500 V/cm and is Shown in the Format of Mean and Variance

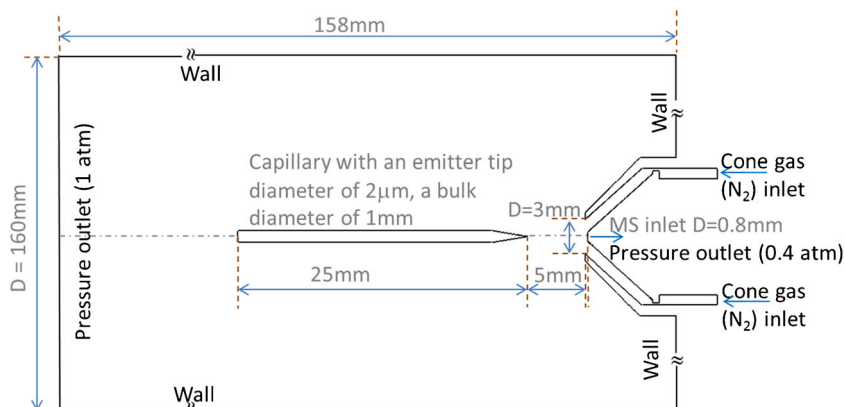| Ion mass (Da)	Ω (Å^2) Collision cross-section	K_0 [cm^2/(V sec)] Estimated by the Mason-Schamp equation	Simulated by the hard sphere collision model	Simulated by the drag model
70	103.5	2.42	2.56±0.02	2.63±0.01
455	210.0	1.04	1.10±0.01	1.13±0.01

Figure 2. Geometry of the axisymmetric nanospray model. Top half above the symmetry line represents the computational domain

simulation results also show that the axial velocities have similar profiles and are directed towards the MS inlet (positive velocity values) for cone gas flow rates lower than 250 slph. For cone gas flow rates greater than 250 slph, the axial flow in most of the ion transport region reverses in the direction (negative values) towards the emitter and the velocity magnitude increases with increasing cone gas flow rates. Simulation results show that a cone gas flow rate of about 250 slph is critical, as it creates an almost stagnant flow in most of the ion transport region. In the experimental study, cone gas flow rates of ≤250 slph were also observed to be crucial for high ion signal intensity. The temperature change mainly occurs within 0.5 mm from the MS inlet and, at the MS inlet, it decreases to 255 K (–18 °C) in this study.

Electric Field

The electric potential distribution depends on the applied voltage on the emitter, the ion source chamber geometry, and the instantaneous charge density distribution. When the geometry
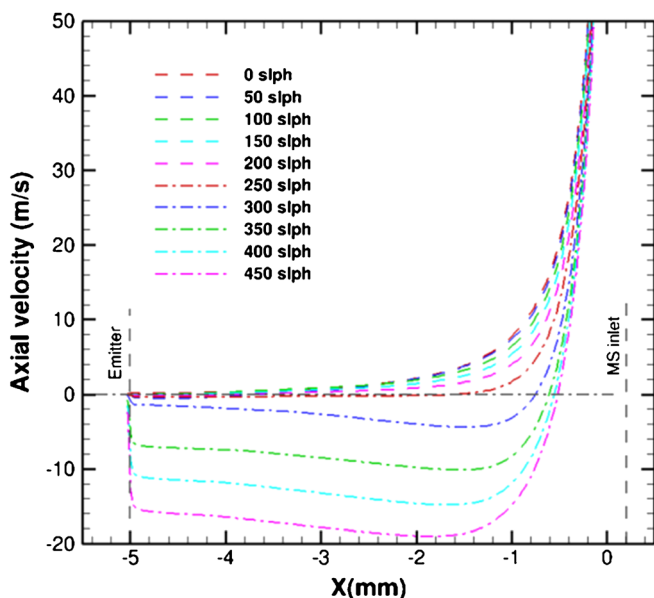

Figure 3. Dependence of the axial velocity profile on the cone gas flow rate

remains unchanged, the real-time electric field is determined by the voltage of the capillary, the ion source current, and the ion distribution.

For a fixed capillary voltage of 2 kV, the ion source current will determine the electric field intensity. Figure 4a and b show the profiles of axial (E_x) and radial (E_r) electric field intensity along the axial direction at $r = 0.2$ mm (1/2 R_{MS}, R_{MS} is the radius of the MS inlet orifice) with a cone gas flow rate of 50 slph and a capillary voltage of 2 kV. The profiles show a rapid reduction of the electric field strength within 0.5 mm of the emitter tip. Increasing the ion source current leads to a valley of the axial field minimum near to the emitter tip due to the effects of ion shielding. On the other hand, higher ion source currents (>30 nA) are shown to give rise to higher axial fields in the majority of the ion transport region (–4 to 0 mm) after recovery from a valley minimum. In this main ion transport region, the axial electric field strength is approximately doubled when increasing the ion source current from 10 to 90 nA, while the radial electric field also increases, but to a lesser extent. This means that a higher source current enhances both the space-charge repelling effect (dispersion) and the ion velocity towards the MS inlet. These two effects, which tend to counteract each other, have the net effect of decreasing the ion transmission efficiency with an asymptotic trend in the current study, which will be discussed later in the section on ion transmission efficiency. Figure 4e shows contour plots for the axial and radial electric fields and gives a two-dimensional perspective on the extent of the fields at various ion source currents. The contours show clearly a stronger electric-field screening with a higher ion source current near the emitter. The distribution of ions introduces a charge source to distort the static field, and the distortion with a higher ion source current is stronger and expands to a larger plume. The influence of capillary voltage on the electric field profiles for a fixed ion source current of 30 nA and a cone gas flow rate of 50 slph is shown in Figure 4c and d. When the voltage on the capillary increases from 1 to 3 kV, electric field intensities in both directions show a quasi-linear growth near the capillary tip. With a lower capillary voltage, the ion velocity in the vicinity of the emitter tip will be lower, leading to a higher concentration of ions in this region. This, in turn, results in a stronger shielding effect and a valley in
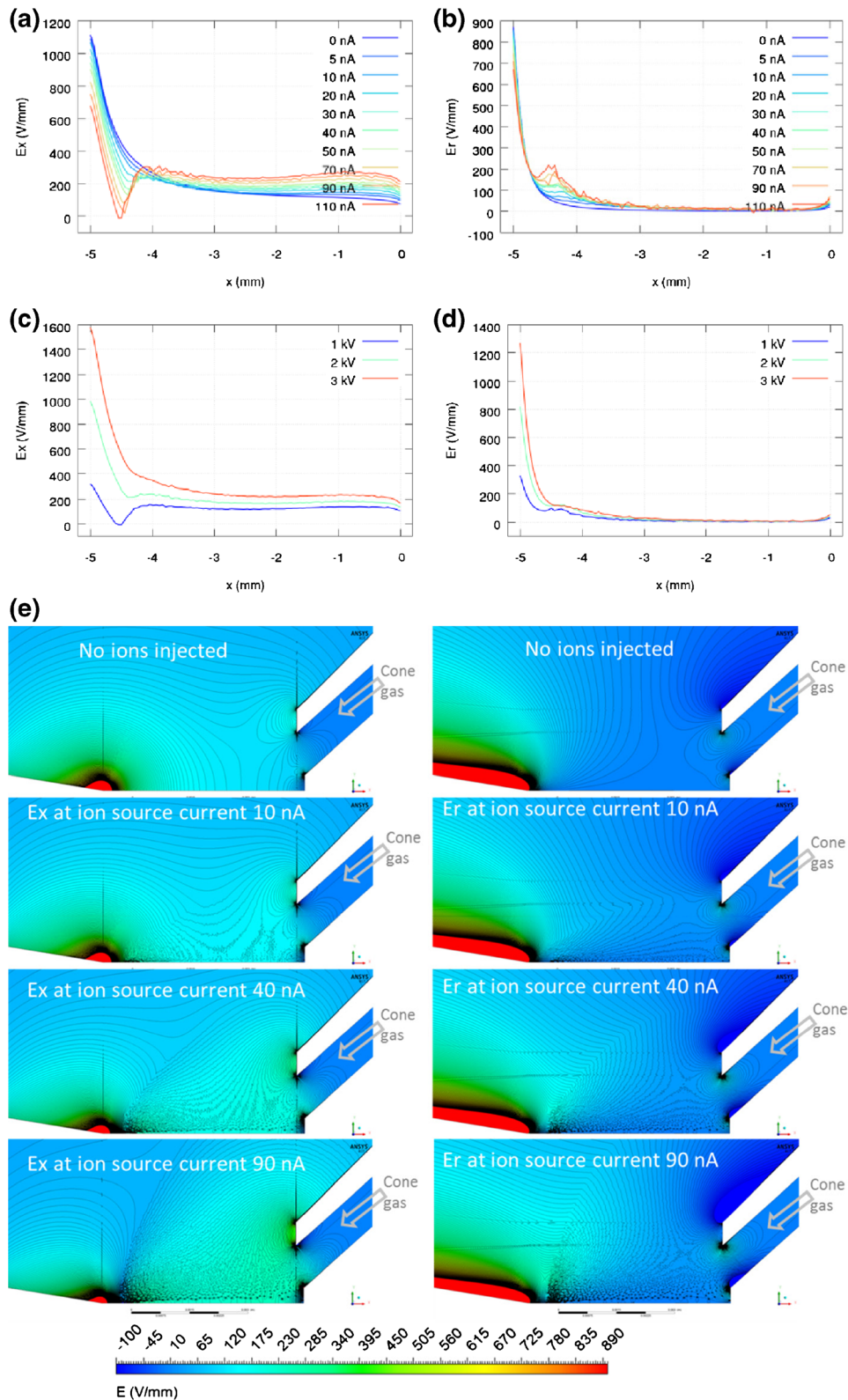
Figure 4. **(a)** Profiles of electric field intensity in the axial direction E_x at $r = 0.2$ mm with different ion source currents (2 kV capillary voltage). **(b)** Profiles of electric field intensity in the radial direction E_r at $r = 0.2$ mm with different ion source currents (2 kV capillary voltage). **(c)** Profiles of electric field intensity in the axial direction E_x at $r = 0.2$ mm with different capillary voltages (30 nA source current). **(d)** Profiles of electric field intensity in the radial direction E_r at $r = 0.2$ mm with different capillary voltages (30 nA source current). **(e)** Contours of the electric field strength in the axial direction E_x (left column) and in the radial direction E_r (right column) at different ion source currents (from top to bottom: 0 nA, 10 nA, 40 nA, 90 nA)
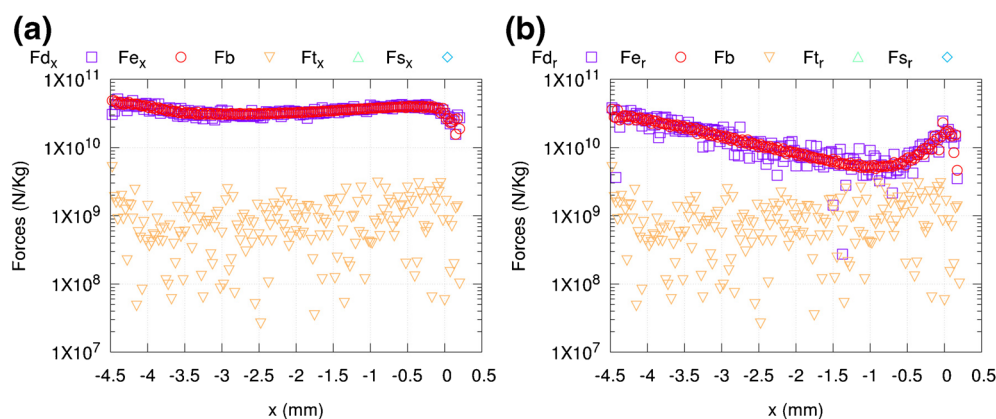
Figure 5. Axial distribution of force magnitudes per unit mass on ions. **(a)** Forces in the axial direction, **(b)** forces in the radial direction. The ions considered herein lie in the main transport region, i.e., −4.5 mm < x < 0.2 mm and the radius r < 1.5 mm. A centered moving average is applied to all forces with a sample window of $\Delta x = 0.025$ mm and $\Delta r = 1.5$ mm

the axial electric field profile. However, as the electric field intensity profiles level from x = −4 to 0 mm, the increase in field strength and, hence, the electric force on the ions becomes small (for example, ~25% increase from 1 to 3 kV).

Comparison of Forces on Ions

In order to improve the accuracy of MS source simulations, it is necessary to consider the relative importance of all the dominant forces on the ions. In this section, a typical nano-ESI spray case with an ion source current of 30 nA, a cone gas flow rate of 50 slph and a capillary voltage of 2 kV is considered.

The corrected drag force and electric forces have been described in the previous section. Additional forces on the ion particle include: (a) a thermophoretic force that is linearly dependent on the normalized temperature difference $\Delta T/T$; (b) a Brownian force that is corrected with a Cunningham factor; (c) a Saffman lift force that is a shear lift originating from the inertia effects in the viscous flow around the particle. The turbulence dispersion of ions is predicted by the stochastic tracking method. When particle rotation in the fluid is not considered, the Magnus lift force and the rotation lift force can be neglected. As the particle density of the ion is much higher than the buffer gas (nitrogen) density, the "virtual mass" force to accelerate the surrounding fluid and the pressure gradient forces are negligible. The definition and physical meanings of these forces can be found in [26, 54, 55].

Figure 5 shows the magnitude of forces per unit mass on ions in both the axial and the radial directions. Let us first consider the axial forces. For the main transport region (−4 mm < x < −1 mm), the drag force, Fd_x, and the electric force, Fe_x, are two dominating forces, which are approximately one order greater than the Brownian force, Fb. The thermophoretic force, Ft_x, is excluded from the shown data range as it is about 8–9 orders smaller than the two dominant forces. The Saffman lift force on the ions, Fs_x, is also negligibly small, as there is no viscous effect from the buffer gas to generate a shear lift force because of the extremely large particle Knudsen number of the gas-phase ions. In conclusion, the dominating forces in the

axial direction are the drag force and the electric force, whereas the Brownian force plays a secondary role. The Saffman lift force and the thermophoretic force are negligibly small. Considering the radial forces shown in Figure 5b, the dominating forces are the drag force, Fd_r, the electric force, Fe_r, and the Brownian force, Fb. Similar to the axial direction, the Saffman lift force, Fs_r, and the thermophoretic force, Ft_r, are, again, too small to be included in the figure. In summary, the drag force, the electric force and the Brownian forces are the top three forces to be considered for an accurate ion transport simulation in a nano-ESI spray. The Saffman lift force, the thermophoretic force, and the turbulence dispersion were included in this study for completeness.

Ion Transmission

Ion transmission efficiency is an important parameter to study since it correlates directly to the MS sensitivity. First, the simulated ion transmission efficiency to the experimental measurements will be compared. Figure 6a compares the normalized ion transmission efficiency of verapamil (m/z 455, charge +1) at different cone gas flow rates. The normalized ion transmission efficiency is defined as the ion transmission efficiency normalized to that obtained with a zero cone gas flow rate. For gas-phase ions with a source current of 30 nA, the simulation results agree reasonably well with the experimental measurements for cone gas flow rates between 0 and 250 slph where the axial flow velocity is very low for most of the ion transport region. However, the discrepancy becomes apparent with a further increase in cone gas flow rates where the experimental data is shown to exhibit a greater decrease in ion transmission with increasing cone gas flow compared with the simulation data. Considering the high probability of the existence of very fine charged droplets in the nanospray plume, simulations of droplets with a fixed diameter of 0.1 µm and a charge of 44% [4] of the Rayleigh limit were carried out to demonstrate the influence of particle size. Figure 6a includes two data sets from droplet simulations,
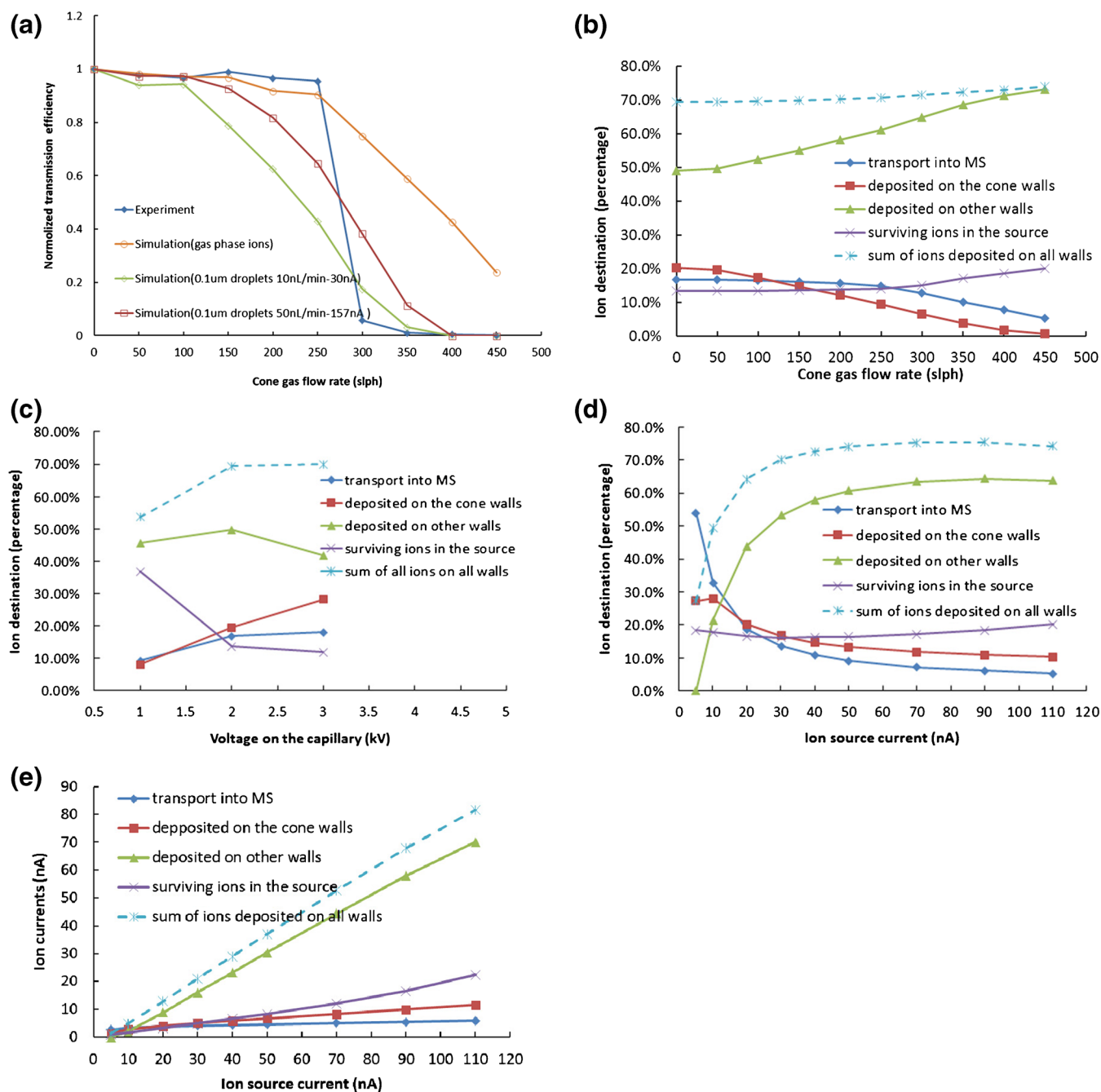
Figure 6. **(a)** A comparison of experimental and simulation results of the normalized ion transmission efficiency at different cone gas flow rates. **(b)** Ion destination at different cone gas flow rates with a fixed source current of 30 nA and a capillary voltage of 2 kV. **(c)** Ion destination at different capillary voltage with a fixed source current of 30 nA and a cone gas flow rate of 50 slph. **(d)** Ion destination at different source currents with a fixed cone gas flow rate of 50 slph and a capillary voltage of 2 kV. **(e)** Total ion current as a function of different source currents with a fixed gas flow rate of 50 slph and a capillary voltage of 2 kV

one with an injection flow rate of 10 nL/min corresponding to a 30 nA source current, and the other with an injection flow rate of 50 nL/min corresponding to a 157 nA source current. The injection flow rates and ion currents are consistent with the characteristics of the PicoTip[TM] emitter used in the experiments. The simulation results show that the transmission efficiency of charged droplets decreases at a significantly greater rate than that observed with gas-

phase ions for cone gas flow rates higher than 200 slph. The experimental data sit between the results for the gas-phase ions and 0.1 μm droplets, which could be expected as it is probable that the particle size will vary between fine droplets and gas-phase ions in real experiments. Besides, Banerjee and Mazumdar [4] summarized that the average lifetime of a charged ESI droplet is around one to a few milliseconds for typical ESI-MS, and the
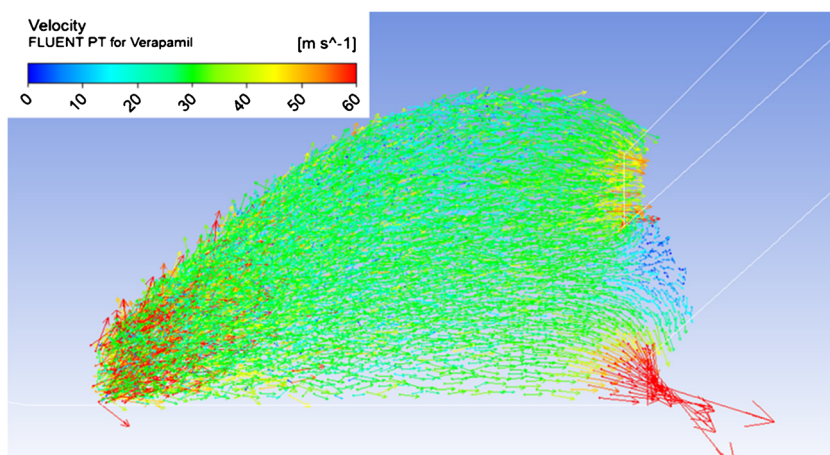
Figure 7. Snapshot of the ion distribution with velocity vectors, colored by velocity magnitude at a cone gas flow rate of 150 slph and source current of 30 nA. (Axisymmetric model)

evaporation timescale for a 0.1 μm droplet is around 40 μs for a microelectrospray process, which is about one-third of a typical transmission time from the source to the MS inlet. This confirms the existence of fine droplets in a nano-ESI source. In the current source configuration, the ion destinations are (1) traveling through the MS inlet (transport into the MS), (2) depositing on the cone walls, (3) depositing on all other walls, and (4) surviving (lingering) in the source chamber. Surviving ions are defined as those that are still being tracked and are not lost by any of the above means at a snapshot in time. The ion destinations are dependent on the cone gas flow rate, the source current, and the capillary voltage. These dependencies have been considered in the present study.

The influence of the cone gas flow rate on the ion destinations is plotted in Figure 6b. When the cone gas flow rate is less than 250 slph, changes to the buffer gas flow only redistribute the ion loss between deposition on the cone wall and on the other walls, and have little influence on the total ion loss, ion transmission, and the ion concentration in the chamber. When the cone gas flow rate is greater than 250 slph, the buffer gas becomes counter-flowing (an opposing force for the ion transport), where the stronger cone gas slows ion transport towards the MS inlet and increases the number of surviving ions in the source chamber, corresponding to enhanced space-charge effects and increased ion dispersion. The ion transmission efficiency into the MS decreases from 16% to 4% when the cone gas flow rate increases from 250 to 450 slph. Since the total source current is fixed in all these cases, the trend of the current into the MS is equivalent to the ion transmission efficiency. The ion current into the MS with a flow rate less than 250 slph is approximately 5 nA, whereas it reduces to around 1 nA with a flow rate of 450 slph.

The influence of the capillary voltage on the ion destination is shown in Figure 6c. For a cone gas flow rate of 50 slph and a source current of 30 nA, the ion transmission efficiency almost doubles for an increase in capillary voltage from 1 to 2 kV, but the enhancement is less marked from 2 to 3 kV. This trend is accompanied by a dramatic reduction in the number of surviving ions in the source from 1 to 2 kV and only a slight decrease from 2 to 3 kV. Less sensitivity to a higher voltage was also observed in [56]. The reason is mainly that a lower capillary voltage generates a smaller electric driving force for ions, leading to a higher ion concentration under continuous ion injection and, in turn, to greater space-charge ion losses. However, the benefit of an increased driving force (capillary voltage) is not boundless, since the shrinking plume and increasing ion concentration is counterbalanced by increased space-charge that ultimately leads to a dynamic equilibrium. This accounts for the observed flattening of the response for ions transported in the MS at increasing capillary voltages (shown in Figure 6c).

The influence of the ion source current on the transmission efficiency at a fixed cone gas flow rate of 50 slph has also been studied, and the computed results are shown in Figure 6d and e. An increase in the source current enhances the space-charge effects and encourages ion dispersion. At the same time, the increased ion concentration in the chamber promotes an enhanced electric driving force for ions in the main transport path (Figure 4a), which reduces the time duration of ion dispersion. As a result of these competing effects, the simulations show that the ion transmission efficiency decreases exponentially with increasing source current, but the total ion current into the MS increases slowly from 3 nA at a source current of 10 nA to 6 nA at a source current of 110 nA (Figure 6e). This trend of an exponential decrease of the ion transmission was also observed in other types of MS [57].

Summarizing the above analysis, the basic mechanism of ion transport depends on the interaction between the assisting forces, the opposing forces, and ion dispersion. Stronger driving/assisting forces (e.g., the buffer gas with a cone gas flow rate of less than 250 slph and the electric force) speed the transport of ions and reduce ion concentration in the source chamber, corresponding to smaller space-charge effects on ion dispersion and ion loss. Opposing forces (e.g., cone gas flow rates greater than 250 slph) have an opposite effect. The ion
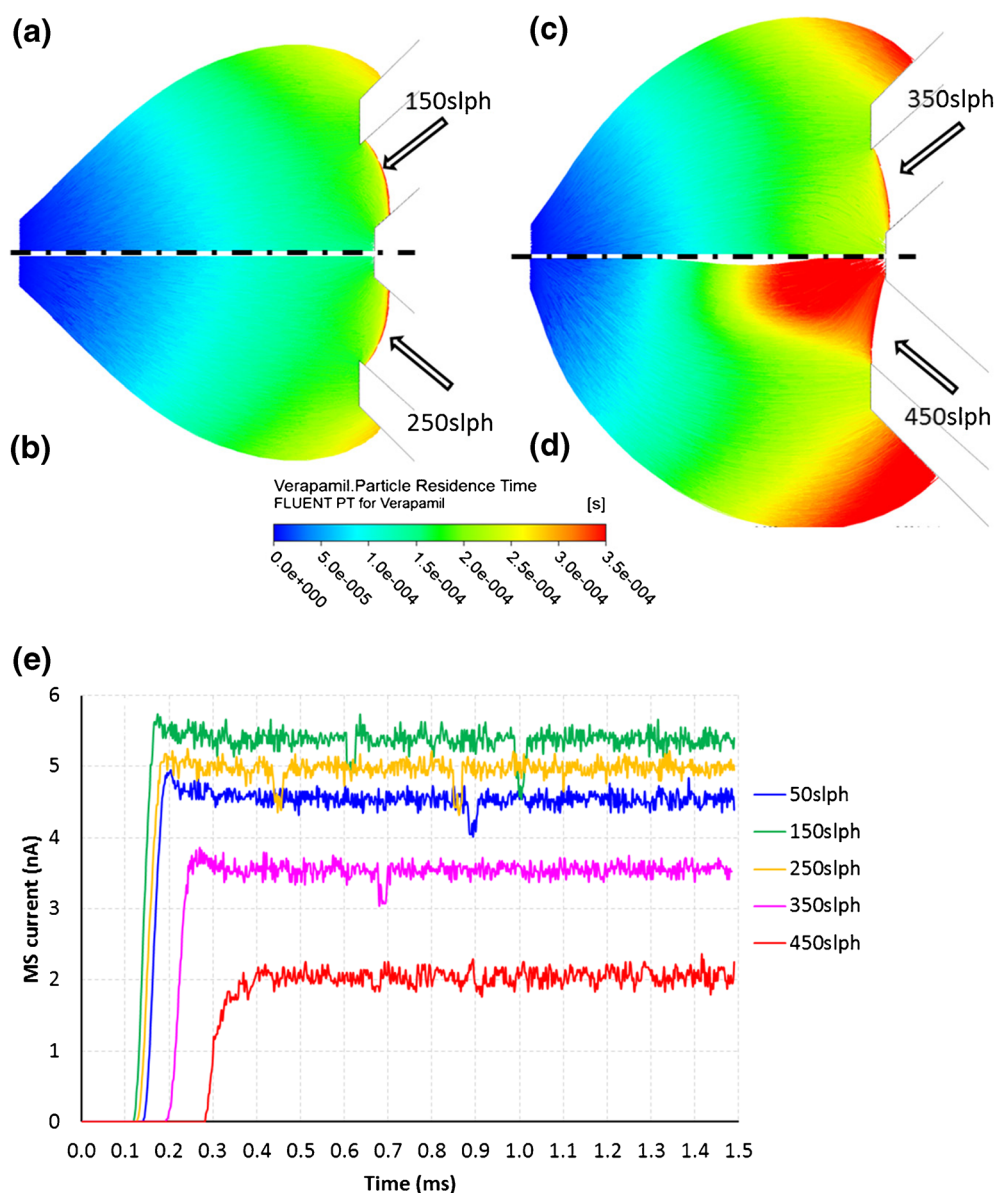
Figure 8. Ion trajectories colored by the ion residence time at a fixed source current of 30 nA and cone gas flow rates of **(a)** 150 slph, **(b)** 250 slph, **(c)** 350 slph, **(d)** 450 slph. **(e)** Time evolution of the ion current through the MS inlet with a source current of 30 nA

dispersion mainly comes from the space-charge effects, which depends on the ion concentration (or charge density). However, factors that increase the number of surviving ions in the source (e.g., a higher ion source current, a weaker driving force, or stronger opposing force) do not promote a linear increase of the ion concentration due to the expansion of the ion plume under the influence of space-charge. Thus, the ion dispersion and ion loss in the ion source chamber has a feature of self-confinement to some extent, which explains the asymptotic characteristics of the ion transmission efficiency under reduced cone gas flow rates, increased capillary voltage, and increased ion source current. In all, for this study, it is observed that a reasonable balance between high transmission efficiency and useful MS signal is obtained at a cone gas flow rate not exceeding 250 slph, a capillary voltage of about 2 kV, and a source current of

between 30 and 40 nA. These observations agree with empirical optimization of typical experimental settings.

In addition to the ion transmission efficiency, details of the ion transport characteristics in the ion source are also revealed in this study. The ion distribution and its velocity at a cone gas flow rate of 150 slph and a source current of 30 nA are shown in Figure 7. For the majority of ions, the mean transport velocity is around 20–40 m/s, whereas the ion velocity is much higher near their initial location due to a higher electric field and initial velocity (refer to Figure 4), and also near the MS inlet due to the stronger axial flow velocity (refer to Figure 3). As a result of the cone gas counterflow, ions entering into the cone almost stagnate there.

In order to demonstrate the cone gas effects on the ion transport, contours of the ion residence time at different cone

gas flow rates are shown in Figure 8a–d. A stronger cone gas flow rate slows the movement of ions and results in a longer transmission time for all ions in the source chamber. Simultaneously, the size of the ion plume expands to cause more ion loss on the chamber walls. The strong cone gas flow of 450 slph significantly slows down the ions near the MS inlet, resulting in more lingering ions in the chamber, as shown in Figure 6b.

Figure 8e shows the evolution of the ion current through the MS inlet from an initial injection at $t = 0$ s for the continuous injection of ions at different cone gas flow rates. The ion signal is recorded every 0.002 ms and a centered moving average running at a time interval of 0.02 ms is applied to smooth signals. The time taken to reach an equilibrium current is longer for higher cone gas flow rates. Having established an equilibrium current, it is found that the ion transmission time is around 0.2 ms for cone gas flow rates of less than 250 slph. A further increase of the cone gas flow rate leads to a longer transmission time, for example, 0.4 ms for a cone gas flow rate of 450 slph. The dynamic process of reaching an equilibrium state also implies that a continuous injection of ions is necessary to obtain realistic ion transport characteristics.

Conclusion

In this study, ANSYS Fluent was customized to simulate flow fields, electric fields, and ion transport in a nanospray ion source under different operating conditions. The particle-in-cell method was implemented to take into account the local real-time charge density. The real-time space-charge effects on electric field distortion and ion transport characteristics in a continuous ion injection mode have been numerically studied. A drag model with the Cunningham slip correction factor has been validated to accurately predict ion transport properties at atmospheric pressure conditions based on a comparison with an ion-gas hard sphere collision model. After comparing the five main types of forces on ions, it was found that the drag force, the electric force, and the Brownian force are the dominating influences, whereas the thermophoretic force and the Saffman lift force are negligibly small for most of the ion transport path. Ion transmission efficiency and ion destinations have been studied at different cone gas flow rates, different source currents, and different capillary voltages, and the computed results reveal valuable insights. Both the experimental and simulation results show that cone gas flow rates of ≤250 slph are necessary for high ion transmission efficiency, as higher cone gas flow rates reduce the ion signal significantly. The computed results also show that the ion transmission efficiency reduces exponentially with an increased ion source current. In this study, only gas-phase ions (and droplets with fixed diameters) are simulated. The developed code in this study also provides a framework to simulate droplets with a given initial diameter and charge distribution for investigating droplet desolvation and transport in a standard ESI source, which will be carried out in a future work.

References

1. Pramanik, B.N., Ganguly, A.K., Gross, M.L.: Applied electrospray mass spectrometry. Marcel Dekker, Inc., New York (2002)
2. Cole, R.B.: Electrospray and MALDI mass spectrometry: fundamentals, instrumentation, practicalities, and biological applications. Wiley, New Jersey (2010)
3. Schneider, B.B., Nazarov, E.G., Londry, F., Vouros, P., Covey, T.R.: Differential mobility spectrometry/mass spectrometry history, theory, design optimization, simulations, and applications. Mass Spectrom. Rev. 35, 687–737 (2016)
4. Banerjee, S., Mazumdar, S.: Electrospray ionization mass spectrometry: a technique to access the information beyond the molecular weight of the analyte. Int. J. Anal. Chem. 2012, 40 pages (2012) https://www.hindawi.com/journals/ijac/2012/282574/
5. Juraschek, R., Dülcks, T., Karas, M.: Nanoelectrospray – more than just a minimized-flow electrospray ionization source. J. Am. Soc. Mass Spectrom. 10, 300–308 (1999)
6. Gapeev, A., Berton, A., Fabris, D.: Current-controlled nanospray ionization mass spectrometry. J. Am. Soc. Mass Spectrom. 20, 1334–1341 (2009)
7. Wright, S., Syms, R.R.A., Moseley, R., Hong, G., O'Prey, S., Boxford, W.E., Dash, N., Edwards, P.: MEMS-based nanospray-ionization mass spectrometer. J. Microelectromech. Syst. 19, 1430–1443 (2010)
8. Karas, M., Bahr, U., Dülcks, T.: Nano-electrospray ionization mass spectrometry: addressing analytical problems beyond routine. Fresenius J. Anal. Chem. 366, 669–676 (2000)
9. Page, J.S., Kelly, R.T., Tang, K., Smith, R.D.: Ionization and transmission efficiency in an electrospray ionization-mass spectrometry interface. J. Am. Soc. Mass Spectrom. 18, 1582–1590 (2007)
10. Cech, N.B., Enke, C.G.: Practical implications of some recent studies in electrospray ionization fundamentals. Mass Spectrom. Rev. 20, 362–387 (2001)
11. Covey, T.R., Thomson, B.A., Schneider, B.B.: Atmospheric pressure ion sources. Mass Spectrom. Rev. 28, 870–897 (2009)
12. Gimelshein, S., Lilly, T., Moskovets, E.: Numerical analysis of ion-funnel transmission efficiency in an API-MS system with a continuum/microscopic approach. J. Am. Soc. Mass Spectrom. 26, 1911–1922 (2015)
13. El-Shafie, M.Y., Bebawi, S., Zomor, H.H., Gunzer, F.: Improvement of the ion transfer efficiency in ion mobility spectrometry-mass spectrometry. 2016 I.E. Workshop on Environmental, Energy, and Structural Monitoring Systems (EESMS). Bari, Italy, June 13-14 (2016)
14. Page, J.S., Marginean, I., Baker, E.S., Kelly, R.T., Tang, K., Smith, R.D.: Biases in ion transmission through an electrospray ionization-mass spectrometry capillary inlet. J. Am. Soc. Mass Spectrom. 20, 2265–2272 (2009)
15. Cox, J.T., Marginean, I., Smith, R.D., Tang, K.: On the ionization and ion transmission efficiencies of different ESI-MS interfaces. J. Am. Soc. Mass Spectrom. 26, 55–62 (2014)
16. Krutchinsky, A.N., Padovan, J.C., Cohen, H., Chait, B.T.: Maximizing ion transmission from atmospheric pressure into the vacuum of mass spectrometers with a novel electrospray interface. J. Am. Soc. Mass Spectrom. 26, 649–658 (2015)
17. Mayer, T., Borsdorf, H.: Ion transfer from an atmospheric pressure ion funnel into a mass spectrometer with different interface options:

Simulation-based optimization of ion transmission efficiency. Rapid Commun. Mass Spectrom. **30**, 372–378 (2016)

18. Zheng, Q., Wei, G.W.: Poisson-Boltzmann-Nernst-Planck model. J. Chem. Phys. **134**, 1–17 (2011)

19. Wissdorf, W.: Simulation of ion dynamics in atmospheric pressure ionization sources. PhD Dissertation University Wuppertal (2014)

20. Landau, D.P., Binder, K.: A guide to Monte-Carlo similations in statistical physics. Cambridge Univesrty Press, Cambridge (2009)

21. Gimelshein, N., Gimelshein, S., Lilly, T., Moskovets, E.: Numerical modeling of ion transport in an ESI-MS system. J. Am. Soc. Mass Spectrom. **25**, 820–831 (2014)

22. Guan, Q., Ellison, G.B., Daily, J.W., Stanton, J.F., Ahmed, M.: DSMC Simulations of a Photoionization Mass Spectrometer. Proceedings of the 54th AIAA Aerospace Sciences Meeting. American Institute of Aeronautics and Astronautics, San Diego, California, January 4 - 8 (2016)

23. Wissdorf, W., Pohler, L., Klee, S., Müller, D., Benter, T.: Simulation of ion motion at atmospheric pressure: particle tracing versus electrokinetic flow. J. Am. Soc. Mass Spectrom. **23**, 397–406 (2012)

24. Zhou, X., Ouyang, Z.: Following the ions through a mass spectrometer with atmospheric pressure interface: simulation of complete ion trajectories from ion source to mass analyzer. Anal. Chem. **88**, 7033–7040 (2016)

25. Lock, C.M., Dyer, E.W.: Simulation of ion trajectories through a high pressure radio frequency only quadrupole collision cell by SIMION 6.0. Rapid Commun. Mass Spectrom. **13**, 422–431 (1999)

26. ANSYS: Fluent Theory Guide. Release 18.0. ANSYS, Inc. Canonsburg, PA (2017)

27. Appelhans, A.D., Dahl, D.A.: SIMION ion optics simulations at atmospheric pressure. Int. J. Mass Spectrom. **244**, 1–14 (2005)

28. Dahl, D.A., McJunkin, T.R., Scott, J.R.: Comparison of ion trajectories in vacuum and viscous environments in SIMION: insights for instrument design. Int. J. Mass Spectrom. **266**, 156–165 (2007)

29. Jarvas, G., Guttman, A., Foret, F.: Numerical modeling of capillary electrophoresis-electrospray mass spectrometry interface design. Mass Spectrom. Rev. **34**, 558–569 (2015)

30. Xu, J., Whitten, W.B.: Monte Carlo simulation of ion transport in ion mobility spectrometry. Int. J. Ion Mobil. Spectrom. **11**, 13–17 (2008)

31. Jurcicek, P., Liu, L., Zou, H.: Numerical simulation of Monte Carlo ion transport at atmospheric pressure within improved air amplifier geometry. Int. J. Ion Mobil. Spectrom. **17**, 157–166 (2014)

32. Zhou, X., Ouyang, Z.: Flowing gas in mass spectrometer: method for characterization and impact on ion processing. Analyst. **139**, 5215–5222 (2014)

33. Manura, D., Dahl, D.: SIMION (R) 8.0 User Manual. Scientific Instrument Services, Inc., Ringoes (2008)

34. Appelhans, A.D., Dahl, D.A.: Measurement of external ion injection and trapping efficiency in the ion trap mass spectrometer and comparison with a predictive model. Int. J. Mass Spectrom. **216**, 269–284 (2002)

35. Ding, L., Sudakov, M., Kumashiro, S.: A simulation study of the digital ion trap mass spectrometer. Int. J. Mass Spectrom. **221**, 117–138 (2002)

36. Langejuergen, J., Cochems, P., Allers, M.: Using COMSOL to build a transient model of a drift tube ion mobility spectrometer with improved performance. Proceedings of the 2011 COMSOL Conference, Stuttgart, Germany, October 26-28 (2011)

37. Langejuergen, J., Cochems, P., Zimmermann, S.: Results of a transient simulation of a drift tube ion mobility spectrometer considering charge repulsion, ion loss at metallic surfaces, and ion generation. Int. J. Ion Mobil. Spectrom. **15**, 247–255 (2012)

38. Han, F., Du, Y., Cheng, S., Zhou, Q., Chen, C.: Keyonghou, Wang, W., Li, H.: Computational fluid dynamics-Monte Carlo method for calculation of the ion trajectories and applications in ion mobility spectrometry. Int. J. Mass Spectrom. **309**, 13–21 (2012)

39. Skoblin, M.G., Chudinov, A.V., Sulimenkov, I.V., Brusov, V.S., Makarov, A.A., Wouters, E.R., Kozlovskiy, V.I.: Numerical simulation of ion transport in an atmosphere-to-vacuum interface taking into account gas dynamics and space charge. Eur. J. Mass Spectrom. **23**, 187–191 (2017)

40. Karypis, G.: METIS A software package for partitioning unstructured graphs, partitioning meshes, and computing fill-reducing orderings of sparse matrices, ver. 5.1.0. University of Minnesota, Minneapolis (2013)

41. Ringle, R.: 3DCylPIC – A 3D particle-in-cell code in cylindrical coordinates for space charge simulations of ion trap and ion transport devices. Int. J. Mass Spectrom. **303**, 42–50 (2011)

42. Mädler, L., Friedlander, S.K.: Transport of nanoparticles in gases: overview and recent advances. Aerosol Air Qual. Res. **7**, 304–342 (2007)

43. Wang, S.M., Inthavong, K., Wen, J., Tu, J.Y., Xue, C.L.: Comparison of micron- and nanoparticle deposition patterns in a realistic human nasal cavity. Respir. Physiol. Neurobiol. **166**, 142–151 (2009)

44. Cunningham, E.: On the velocity of steady fall of spherical particles through fluid medium. Proc. Royal Soc. A Math. Phys. Eng. Sci. **83**, 357–365 (1910)

45. Li, Z., Wang, H.: Drag force, diffusion coefficient, and electric mobility of small particles. I. Theory applicable to the free-molecule regime. Phys. Rev. E Stat. Nonlinear Soft Matter Phys. **68**, 61206 (2003)

46. Clift, R., Grace, J.R., Weber, M.E.: Bubbles, drops and particles. Academic Press, Inc., New York (1978)

47. Campuzano, I., Bush, M.F., Robinson, C.V., Beaumont, C., Richardson, K., Kim, H., Kim, H.I.: Structural characterization of drug-like compounds by ion mobility mass spectrometry: comparison of theoretical and experimentally derived nitrogen collision cross sections. Anal. Chem. **84**, 1026–1033 (2012)

48. Revercomb, H.E., Mason, E.A.: Theory of plasma chromatography/gaseous electrophoresis. Rev. Anal. Chem. **47**, 970–983 (1975)

49. Mason, E.A., McDaniel, E.W.: Transport properties of ions in gases. Wiley, New York (1988)

50. Smirnov, B.M.: Theory of gas discharge plasma. Springer, Heidelberg (2014)

51. Rohner, T.C., Lion, N., Girault, H.H.: Electrochemical and theoretical aspects of electrospray ionisation. Phys. Chem. Chem. Phys. **6**, 3056 (2004)

52. Gabriel, E., Fagg, G.E., Bosilca, G., Angskun, T., Dongarra, J.J., Squyres, J.M., Sahay, V., Kambadur, P., Barrett, B., Lumsdaine, A., Castain, R.H., Daniel, D.J., Graham, R.L., Woodall, T.S.: Open MPI: goals, concept, and design of a next generation MPI implementation. Proceedings of the 11th European Parallel Virtual Machine and Message Passing Interface Users' Group Meeting. Budapest, Hungary, September 19 - 22 (2004)

53. Skoblin, M., Chudinov, A., Soulimenkov, I., Brusov, V., Kozlovskiy, V.: Gas flow in the capillary of the atmosphere-to-vacuum interface of mass spectrometers. J. Am. Soc. Mass Spectrom. **28**, 2132–2142 (2017)

54. Li, A., Ahmadi, G.: Dispersion and deposition of spherical particles from point sources in a turbulent channel flow. Aerosol Sci. Technol. **16**, 209–226 (1992)

55. Gupta, P.K., Pagalthivarthi, K.V.: A comparative study of the effect of model lift coefficients on particle trajectory. Indian J. Eng. Mater. Sci. **13**, 293–306 (2006)

56. Hoyes, J., Richardson, K.: From solution phase to spectrometer, an analytical model for the electrospray process from a proteomics perspective. Proceedings of the 59th ASMS Conference on Mass Spectrometry and Allied Topics. ID 236926, Denver, Colorado, June 5–9 (2011)

57. Jolliffe, C., Savtchenko, S., Javahery, R.: Understanding the impact of space charge upon the sensitivity of atmospheric ion sampling. Proceedings of the 62nd ASMS Conference on Mass Spectrometry and Allied Topics. ID 244031, Baltimore, Maryland, June 15–19 (2014)